Nanoscale

Accepted Manuscript

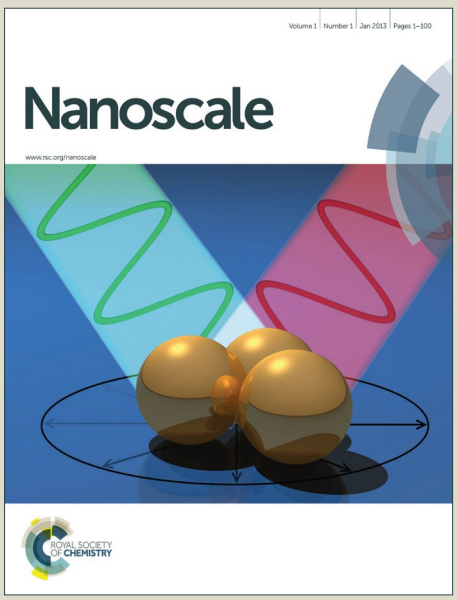

ROYAL SOCIETY OF CHEMISTRY

www.rsc.org/nanoscale

Journal Name

ARTICLE

Polarization State-Based Refractive Index Sensing with Plasmonic Nanostructures

Received 00th January 20xx,
Accepted 00th January 20xx

DOI: 10.1039/x0xx00000x

www.rsc.org/

Shao-Ding Liu,*[a,b] Xin Qi,[a,b] Wu-Chao Zhai,[a,b] Zhi-Hui Chen,[a,b] Wen-Jie Wang,[a,b] and Jun-Bo Han[c]

Spectral-based methods are often used for label-free biosensing. However, practical implementations with plasmonic nanostructures suffer from the broad line width caused by strong radiative and nonradiative losses, and the sensing performance characterized by figure of merit is poor for these spectral-based methods. This study provides a polarization state-based method using plasmonic nanostructures to improve the sensing performance. Instead of the intensity spectrum, the polarization state of transmitted field is monitored to analyze variations of surrounding medium. The polarization state of incidence is strongly modified due to the excitation of surface plasmons, and the ellipticity of transmitted field changes dramatically around plasmon resonances. Sharp resonances with line widths down to one nanometer are achieved by plotting the spectra of the reciprocal of ellipticity. Therefore, the sensing performance can be significantly improved, and a theoretical value of figure of merit exceeding 1700 is achieved by using the polarization state based sensing approach.

Introduction

The remarkable optical responses of metallic nanoparticles are governed by the excitation of localized surface plasmon resonances (LSPRs), where the resonance energy depends on the particle shape, size, composition, interparticle spacing, and dielectric environment.[1-3] These properties open a route toward label-free biosensing in which small concentrations of target molecules can be detected.[4-7] The bulk refractive index sensitivity $\delta\lambda_{LSPR}/\delta n$ is often considered to quantify the sensing performance of a sensor by using plasmonic nanostructures, where δn is the variation of the environment refractive index, and $\delta\lambda_{LSPR}$ is the corresponding spectral shift. Since the line width will strongly affect the final accuracy of the peak tracking, the most crucial sensing performance is characterized by the figure of merit (FoM), obtained by dividing the spectral shift $\delta\lambda_{LSPR}/\delta n$ by the line width of the resonance.[8, 9] The sensing performances with various plasmonic nanoparticles have been investigated, such as nanocubes,[8] nanostars,[10] nanorods,[11-13] nanopillars,[14] nanoprisms,[15] nanodisk dimers,[16] core/shell nanoparticles,[17] nanorings,[18] split-rings,[19, 20] and asymmetric double split-rings.[21] The spectral shift sensitivity can be as large as 880 nm per refractive index unit (nm/RIU),[18] and FoM exceeding 10 is realized by using single nanoparticles.[10] With the excitation of gap plasmon modes, a sensing performance with spectral shift sensitivity exceeding 1000 nm/RIU and FoM exceeding 20 is achieved with double nanopillars.[22] However, due to the strong radiative and non-radiative losses, LSPRs often possess broad line widths, and it is hard to further enlarge the FoM value with these nanostructures.

Fortunately, the line width of LSPRs can be effectively reduced by suppressing radiative losses, and dark plasmon modes with overall dipole moment approaching to zero are promising candidates to improve the sensing performance. Dark plasmon modes can be excited through near-field coupling with bright modes, and destructive interferences often lead to the formation of Fano resonances.[23-31] In this case, radiative damping is suppressed, and the incidence energy can be confined around plasmonic nanostructures effectively, leading to strong near-field enhancements and sharp resonances.[32] Many plasmonic nanostructures with Fano resonances have been used to demonstrate the improved sensing performance, such as ring/disk cavities,[33, 34] rod/cross dimers,[35] nanohole quadrumers,[36] and nanoparticles coupling with substrate.[37] The FoM value is enlarged to 27 by using Fano-like interference in nanorice and nanobelt,[38] and the theoretical FoM value exceeding 40 can be possibly achieved with double ring/disk cavities.[39] It is also reported that molecular monolayers can be identified by using plasmonic Fano resonance,[40] and biomolecules can even be detected with the naked eye.[41] Nevertheless, the line width of Fano resonances is still governed by non-radiative losses. Tremendous efforts aimed at further reducing the line width and improving the sensing performance have been conducted.[42-50] Such as the sensing method with phase sensitive measurements,[44, 45] the intensity-based method with

[a] Key Lab of Advanced Transducers and Intelligent Control System of Ministry of Education, Taiyuan University of Technology, Taiyuan 030024, P. R. China; E-mail: liushaoding@tyut.edu.cn
[b] Department of Physics and Optoelectronics, Taiyuan University of Technology, Taiyuan 030024, P. R. China
[c] Wuhan National High Magnetic Field Center, Huazhong University of Science and Technology, Wuhan 430074, P. R. China

perfect absorber,[46] and the sensing method based on plasmonic interferometry.[47-50] It is shown that the performance of the latter one is comparable to commercial prism-based surface plasmon resonance systems, and the sensing platforms can be achieved with simple transmission geometry, a miniaturized footprint, and a low-cost spectrometer.[47-50] Another effective way is by coupling of LSPRs with modes that possess a smaller line width.[51-55] For example, the FoM value is enlarged to about 58 for a Fabry-Pérot cavity-coupled plasmonic device.[52] Due to the coupling with propagating plasmon resonance, the FoM value is enlarged to 72 for ring/disk cavities on conducting substrates.[53] A FoM value of up to 108 arising from the interference between Wood's anomaly and the LSPRs has been reported for periodic arrays of gold nano-mushrooms.[56] It is, however, worth noting that the geometries of these plasmonic nanostructures could be substantially complex, and the sensing performance is enhanced around a narrow and specific spectral range where resonant coupling occurs.

Not long ago, Maccaferri *et al.* reported a sensing approach based on light phase control by using magnetoplasmonic ferromagnetic nanoparticles, where the ellipticity of incidence is modified by magneto-optical effect, shape resonances appear in the spectra related to the ellipticity, and FoM approaching to 150 is realized.[57] However, the modulation of polarization relies on magneto-optical effect, and a strong external magnetic field is required. Besides that, the chemical stability of ferromagnetic nanoparticles is relatively poor, and the inherent losses are also stronger than that of noble metals. As a result, the spectral shift sensitivity is weaker than that of plasmonic nanostructures. Since the modulation of polarization state is important for this sensing approach, plasmonic nanostructures may be used for the polarization state-based sensing. It has been shown that a linearly polarized wave transmitted through plasmonic nanostructures can become elliptical,[58-61] which is caused by charge transfer effect, and no external magnetic field is required.[62-64] Therefore, the sensing platform can be effective simplified for the polarization state-based method by using plasmonic nanostructures. In addition, the modulation of polarization state and the near-field enhancement highly depend on the excitation of LSPRs, and the sensing performance is expected to be significantly improved.

Results and Discussions

Polarization state modulation. Spectral-based methods are often used for label-free biosensing, where the transmission or reflection spectra are measured with a spectrometer, and variations of surrounding medium such as adsorption of biomolecules are analyzed by monitoring the spectral shift. However, strong radiative and nonradiative losses of plasmonic nanostructures result in a broad line width, and the sensing performance characterized by FoM is poor for these spectral-based methods. This study will show that a polarization state-based method can be used to improve the sensing performance. Figure 1a shows a schematic view of

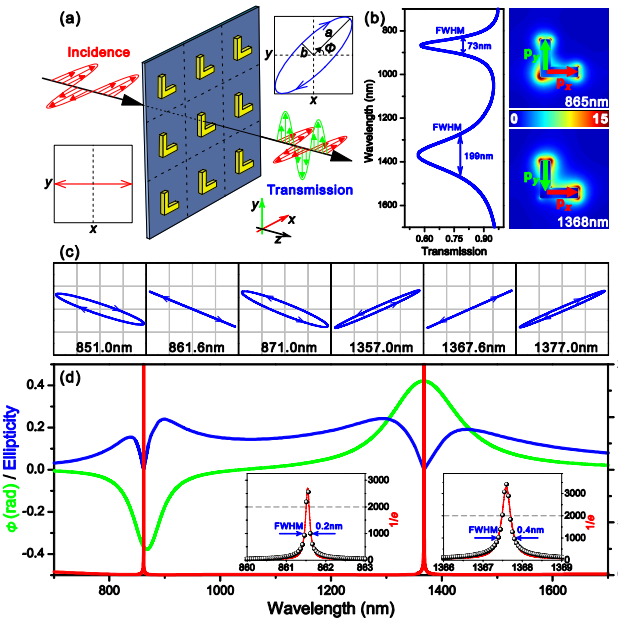

Fig. 1 (a) Schematic view of a polarization state-based sensing platform, where a linearly polarized wave transmitted through the array of L-shaped nanorods becomes elliptical. (b) Transmission spectrum and near-field enhancement distributions around the two resonances. (c) Elliptical polarization states of transmitted waves with different incident wavelengths. (d) Optical polarization rotation (greed solid line), ellipticity *e* (blue solid line), and reciprocal of ellipticity 1/*e* (red solid line) of transmitted field against incident wavelengths. The insets show the magnified 1/*e* spectra around the antibonding and bonding resonances, respectively. The L-shaped nanorods are placed on a semi-infinite glass substrate, the lengths of the two arms are 150 nm, the width is 40 nm, the thickness is 30 nm, the periodicities along both directions are 400 nm, the refractive index of surrounding medium is supposed to be 1.33, and the polarization of incidence is along the *x*-axis.

the sensing platform. The overall configuration is similar as that of spectral-based methods, and there is no need to make a large change to currently used sensing platforms. Nevertheless, several specific criteria should be fulfilled for this sensing approach: (1) a linearly polarized incidence, (2) the polarization state of incidence can be modified by the sensing platform, and (3) the polarization state of modified field is monitored to analyze variations of surrounding medium.

L-shaped gold nanorods will be utilized to demonstrate the sensing performance with the polarization state-based method (Figure 1a), where the lengths of the two arms are 150 nm, the width is 40 nm, the thickness is 30 nm, the periodicities along both directions are 400 nm, and the polarization of incidence is along the *x*-axis. Due to the excitation of surface plasmons, two resonances around 865 and 1368 nm appear in the transmission spectrum (left panel, Figure 1b). The corresponding near-field enhancement distributions are shown on the right panel of Figure 1b. Plasmons oscillate along the arms and over the whole length of the L-shape for the resonances around 865 and 1368 nm, respectively. According to the plasmon hybridization theory,[65] optical responses of the L-shaped nanorod can be seen as plasmon hybridizations between the two arms, and the two resonances are the corresponding antibonding and bonding dipole modes. The overall dipole moments of the two resonances are relatively strong, resulting in broad line widths. The measured line widths of the antibonding and bonding modes are about

and 199 nm, respectively, with a corresponding quality factor of 12 and 7.

In addition to the intensity, the polarization state of transmitted field is modified by the L-shaped nanorods. As shown in Figure 1a and 1b, free electrons are driving by the *x*-polarized incidence, leading to the formation of an effective electric dipole oscillating parallel to the incident polarization ($\mathbf{p}_x$). Besides that, an effective electric dipole oscillating perpendicular to the incident polarization is generated due to the charge transfer effect ($\mathbf{p}_y$). As a result, a linearly polarized wave transmitted through the L-shaped nanorods can become elliptical. The optical polarization rotation is denoted as Φ, and the ellipticity $e = a/b$, where a and b are the short and long semiaxes of the polarization ellipse (Figure 1a). Then, the electric field of the transmitted wave can be written as,

$$\mathbf{E}_t(r,t) = \mathbf{E}_{tx} + \mathbf{E}_{ty} = E_{tx}\cos(kz - \omega t + \varphi_{tx})\vec{x} + E_{ty}\cos(kz - \omega t + \varphi_{ty})\vec{y} \quad (1)$$

and one can get the corresponding polarization state by using,

$$\frac{x^2}{E_{tx}^2} + \frac{y^2}{E_{ty}^2} - 2\frac{\cos\delta}{E_{tx}E_{ty}}xy = \sin^2\delta \quad (2)$$

where the amplitudes E_{tx} and E_{ty} depend on the dipole moments of $\mathbf{p}_x$ and $\mathbf{p}_y$, and $\delta = \varphi_{tx} - \varphi_{ty}$ is the phase difference. Physically, the transmitted polarization state at any wavelength is determined by the dipole moments and the phase difference δ of the two scattering electric dipoles ($\mathbf{p}_x$ and $\mathbf{p}_y$). Since the two dipoles are governed by LSPRs, a null condition with ellipticity $e = 0$ can be realized by manipulating the incident wavelength, where the transmitted field is linearly polarized in this case (δ = 0, π, 2π …). As a result, measuring this null condition provides an alternative way to detect any shift of LSPRs induced by variations of the surrounding medium.

Figure 1c shows several elliptical polarization states of transmitted waves around the two resonances. With the formation of the electric dipole perpendicular to the incident polarization, the optical polarization rotation is strongly modified by incident wavelength, and the rotation angles around the two resonances can be as large as -0.38 and 0.42 radians, respectively (green solid line, Figure 1d). Besides that, the ellipticity of transmitted field changes dramatically around the same spectral ranges (blue solid line, Figure 1d). The wavelength of null conditions can be determined when the ellipticity *e* approaches to zero, and the transmitted waves are almost linearly polarized around 861.6 and 1367.6 nm. It is worth mention that similar null conditions have been investigated for plasmonic interferometry and perfect absorption,[46, 47] which are hard to achieve in real experiments due to the fabrication and measurement errors. Nevertheless, the null condition for the polarization-state based sensing could be determined when the polarization rotation state is considered in a realistic system. One can find that the polarization rotation state of transmitted filed changes from left-hand to right-hand, and vice versa, across the null conditions (Figure 1c). This observation indicates that a sign (+/-) can be attached to the ellipticity *e* to represent the polarization rotation state. Therefore, the fabrication and measurement errors may enlarge the uncertainty, but the null condition can be determined with a curve-fitting method in a realistic system. The corresponding wavelengths can be more precisely visualized by plotting the reciprocal of ellipticity 1/*e* (red solid line, Figure 1d), and we will show that the sensing performance are dramatically improved by plotting the data in this manner. There are two sharp resonances in the spectrum of 1/*e*. In order to better illustrate the two resonances, and to determine the line widths, the spectra around the two resonances are magnified as shown in the inset of Figure 1d. The null condition is governed by the phase difference δ, the peak positions of the 1/*e* spectra and transmission spectra are not bound to be identical, and there is a small wavelength detuning. Since the ellipticity is approaching to 0 around the null condition for an ideal system, the value of 1/*e* should be infinite at the resonance wavelength. However, in the calculations, the value of 1/*e* is limited by the wavelength resolution (0.05 nm), and the maximum value of 1/*e* is only about several thousand. In real experiments, the value of 1/*e* is also limited by experimental errors such as the resolution of polarization analyzer. Therefore, we assume the maximum 1/*e* value of 2000 in the determination of line widths by accounting for experimental errors. This value corresponds to a resolution of ellipticity angle of about 500 micro-radians which is easily achievable for a realistic system (resolution down to submicro-radians). Then, we obtain line widths of about 0.2 and 0.4 nm for the antibonding and bonding resonances, respectively. The quality factors of the two resonances are as large as 4308 and 3419, respectively. Therefore, one can expect that the value of FoM can be significantly enlarged by using the polarization state-based sensing approach.

Bulk refractive index sensitivity. Furthermore, bulk refractive index sensitivity is investigated to characterize the sensing performance. By manipulating the refractive index of surrounding medium, variations of the 1/*e* spectrum for the antibonding and bonding resonances are shown in Figure 2a and 2b, respectively. As a comparison, the dependence of the transmission spectra on the refractive index of surrounding medium is represented in Figure 2c. The resonances shift to lower energies with the increasing of refractive index for both 1/*e* and transmission spectra. However, the spectral shifts can be more easily distinguished using the 1/*e* spectra due to the sharper resonances. The relative spectral shifts against the refractive index are extracted as shown in Figure 2d. The spectral shifts are bound to be identical for both 1/*e* and transmission spectra. A linearly fit for the two sets of data indicates that the spectral shift sensitivities of the antibonding and bonding resonances are, respectively, about 347 and 589 nm/RIU. When the line widths of the two resonances are taken into account, remarkable improvements for FoM performances are achieved by using the polarization state-based method. Due to the broad line widths of the transmission spectra, the calculated FoM is only about 5 and 8 for the antibonding and bonding resonances, respectively. The corresponding FoM are enlarged to about 1735 and 1473 when the 1/*e* spectra are used. Such large spectral shift

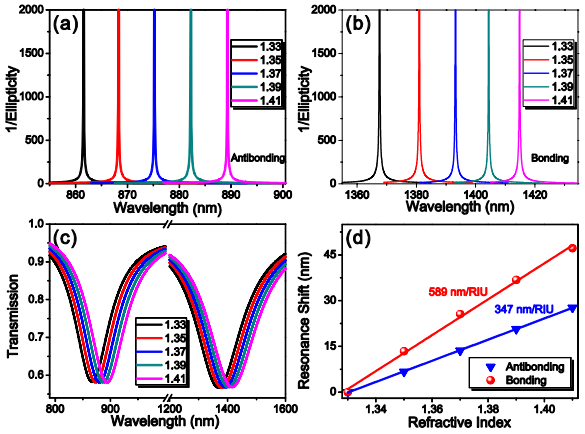

Fig. 2 (a) Plot of the transmitted field 1/*e* spectra with different surrounding media for the antibonding, and (b) bonding resonances. (c) The relationship between the transmission spectrum and the refractive index of surrounding medium. (d) Relative resonance wavelength shifts with the variations of surrounding medium for the two resonances of L-shaped nanorods.

FoM make it possible to detect and distinguish a tiny change of surrounding medium for the polarization state-based sensing approach, while it would be hard to distinguish for spectral-based methods.

Surface sensitivity. For biosensing in a realistic system, target molecules are often adsorbed on the surface of plasmonic nanostructures, which results in local variations of the refractive index. Therefore, the performance of surface sensitivity is important for a sensing platform.[66-68] The surface sensitivity can be characterized by the variations of spectra against the localized refractive index,[34] or against the thickness of molecular layers.[57, 69] In this study, the later one will be used to characterize the surface sensitivity, and the performance can be quantified by defining $S_{surf} = \Delta\lambda/\Delta t$, where $\Delta\lambda$ is the spectral shift due to the changing of the thickness of molecular layer (Δt). In order to have a comparison with previous studies[57], a polyamide 6.6 (PA-6.6) molecular layer is supposed to be coated on the L-shaped nanorods (Figure 3a). The polymer molecules can be attached on samples through molecular layer deposition, and the layer thickness is finely controlled by manipulating deposition cycles. For theoretical studies, the deposited molecules can be seen as a thin dielectric layer, and the corresponding refractive index of PA-6.6 is 1.51.[70] Figure 3b and 3c show the evolutions of 1/*e* spectra against the thickness of the dielectric layer, and the corresponding transmission spectra are shown in Figure 3d. Similar to the bulk refractive index sensing, the two resonances red shift significantly with the increasing of the thickness of dielectric layer, and the spectral shifts also can be more easily distinguished by using the 1/*e* spectra. The extracted data of resonance shifts versus the thickness are represented in Figure 3e, and the linearly fit results indicate that the surface sensitivity for the antibonding and bonding resonances can be as large as 5.1 and 8.9, respectively. The thickness of a monolayer of PA-6.6 is about 8.5 Å, and spectral shifts of about 4.3 and 7.6 nm are expected to be observed for the two resonances when there is a change of a monomolecular layer. Considering the line widths of the 1/*e*

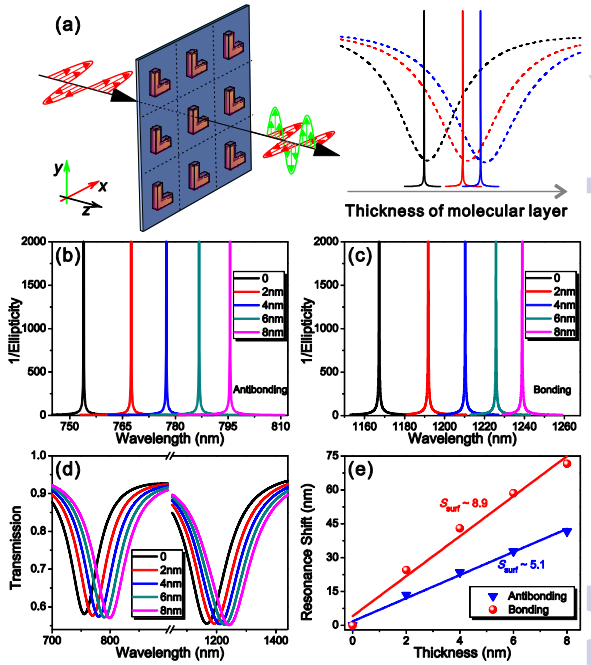

Fig. 3 (a) Schematic view of surface sensing with L-shaped nanorods, where a PA-6.6 molecular layer is supposed to be coated on the L-shaped nanorods (n = 1.51), and the surrounding medium is supposed to be air. (b) Plot of the transmitted field 1/*e* spectra against the thickness of the molecular layer for the antibonding, and (c) bonding resonances. (d) The transmission spectra versus the thickness of the molecular layer. (e) Relative resonance wavelength shifts with the variations of the thickness of the molecular layer.

spectra (0.2 and 0.4 nm for the two resonances), these spectral shifts can be easily distinguished for a realistic sensing platform.

Sensing with nanorod dimers. Since the modulation of polarization state by using plasmonic nanostructures are governed by the structural symmetry, a large group of nanostructures can be used to implement the polarization state-based label-free biosensing. In addition to the L-shaped nanorods (where the structural symmetry belongs to C_{2v} point group), planar plasmonic nanostructures are suitable for this sensing approach when the structural symmetry belongs to C_s, $C_{\infty v}$, C_{2h}, D_{2h}, and $D_{\infty h}$ point groups. It is also well known that hot-spots caused by plasmon interactions are useful to improve the sensing performance. As an example, we will show in the following studies that nanorod dimers can be used to implement the polarization state-based sensing, where the structural symmetry belongs to $D_{\infty h}$ point group (transverse dimensions are neglected), and the sensing performance is further improved due to the formation of strong hot-spot.

The center panel of Figure 4a represents a unit cell of the sensing surface with nanorod dimers, where the dimers are placed on a semi-infinite glass substrate, the dimer orientation is along the *x*-axis, the length of individual nanorods is 140 nm, the width is 40 nm, the thickness is 30 nm, and the gap length is 20 nm. When the incident polarization is along the *x*-axis (polarization angle ϑ = 0), only one effective electric dipole along the same direction is generated, and no polarization rotation and phase modulation can be observed. Noted that the direction of incident polarization is identical with that of a symmetry axis of the dimer, the polarization state cannot

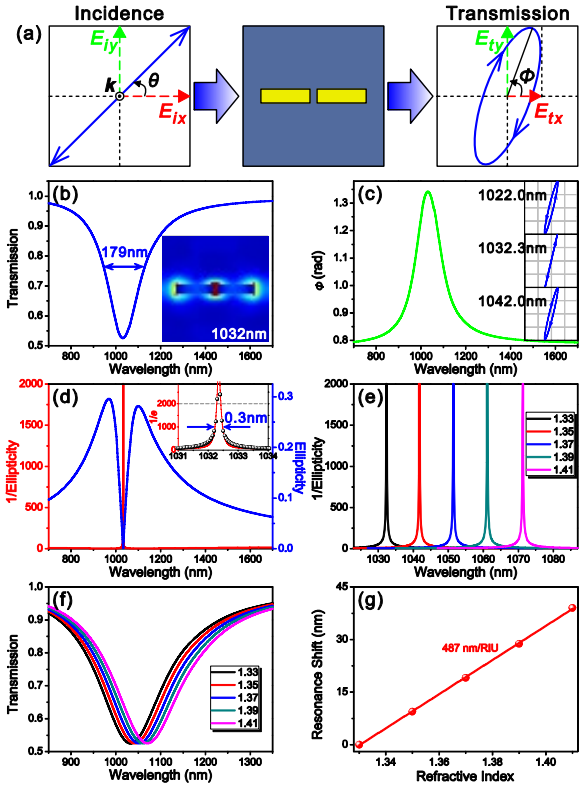

Fig. 4 (a) Schematic view of a polarization state-based sensing platform by using nanorod dimers, where the center panel represents a unit cell of the array, the orientation of the dimers is along the *x*-axis, the length of individual nanorods is 140 nm, the width is 40 nm, the thickness is 30 nm, and the gap length is 20 nm. (b) Transmission spectrum with incident polarization ϑ = 45°, and the inset shows the near-field enhancement distributions around the resonance. (c) Optical polarization rotation spectrum, the insets represent several elliptical polarization states of transmitted waves. (d) ellipticity *e* (blue solid line) and reciprocal of ellipticity 1/*e* (red solid line) of transmitted field against incident wavelengths, and the inset shows the magnified 1/*e* spectrum around the resonance. (e) Plot of the transmitted field 1/*e* spectra, and (f) transmission spectra with different surrounding media. (g) Relative resonance wavelength shifts with the variations of surrounding medium.

modified in this case. Therefore, the incident polarization should be away from structural symmetry axes for the polarization state-based method.

When $\vartheta \neq 0$, the incident electric field can be divided into two non-zero components ($\mathbf{E}_{ix}$ and $\mathbf{E}_{iy}$). The amplitude and phase of $\mathbf{E}_{ix}$ will be strongly modified by the rod dimers around longitudinal LSPRs, while there are minor changes for $\mathbf{E}_{iy}$. As a result, the electric field and the polarization state of transmitted wave also can be described by, respectively, Equ. (1) and Equ. (2), and the polarization state is modified by manipulating the incident wavelength. Figure 4b shows the transmission spectrum with ϑ = 45°, where there is only one resonance around 1032 nm. The inset shows the near-field enhancement distributions and the bonding dipole resonance is excited in this situation. Due to the strong coupling, radiative damping is strong for the bonding dipole mode. The line width is about 179 nm, and the quality factor is only about 6.

The same as the L-shaped nanorods, the polarization rotation is governed by plasmon resonances, and the maximum rotation angle is about 0.55 radians using the nanorod dimers (Figure 4c). The inset of Figure 4c represents several elliptical polarization states of transmitted field around

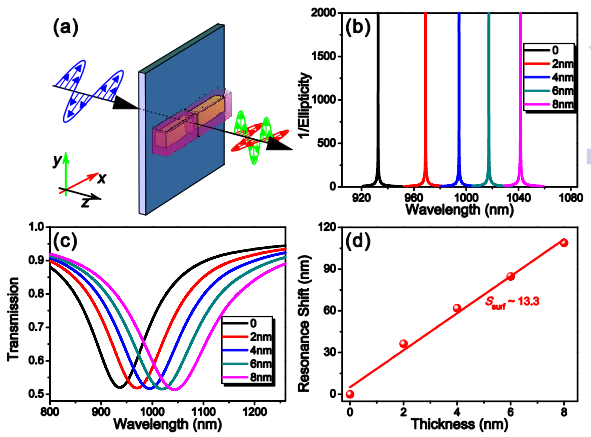

Fig. 5 (a) Schematic view of surface sensing with nanorod dimers, where a PA-6 molecular layer is supposed to be coated on the dimers (n = 1.51), and the surrounding medium is supposed to be air. (b) Plot of the transmitted field 1/ spectra, and (c) transmission spectra against the thickness of the molecular lay (d) Relative resonance wavelength shifts with the variations of the thickness of the molecular layer.

the bonding resonance, and the ellipticity highly depends on incident wavelength. The blue solid line in Figure 4d shows the evolution of ellipticity of transmitted field versus th wavelength. It is found that the ellipticity *e* approaches to zero around 1032.3 nm, and the transmitted field is almost linearl polarized. A sharp resonance appears by plotting the 1/ spectrum (red solid line, Figure 4d). The magnified spectr around the resonance reveals that the line width is less tha 0.3 nm, which leads to a quality factor of about 3441. B manipulating the refractive index of the surrounding medium the resonances of 1/*e* and the transmission spectra red shi simultaneously (Figure 4e and 4f). The data of relative spectra shift against the refractive index are shown in Figure 4g, an the calculated spectral shift sensitivity is about 487 nm/RIU Considering the line width of the spectra, FoM is only about for the spectral-based method, while FoM is enlarged to about 1623 by using the polarization state-based method.

The performances of surface sensitivity with the nanorod dimers are shown in Figure 5, where the incident polarization angle ϑ = 45°, and the coated dielectric layer is the same a that of the L-shaped nanorods. Because of the formation o the strong hot-spot, the performance is expected to be improved. Figure 5b represents the variations of 1/*e* spectra b manipulating the thickness of dielectric layer, and the corresponding transmission spectra are shown in Figure 5 The relative resonance shift exceeds 100 nm when the thickness is enlarged to 8 nm, and the surface sensitivity S_{surf} can be as large as 13.3, which is about 2.5 times the surface sensitivity for ferromagnetic nanoparticles (Figure 5d).[57]

Comparisons with ferromagnetic nanoparticles. In the above studies, the transmitted field is used for the polarization state based sensing. Nevertheless, one can get similar results b using the reflected field. Since the spectral shift sensitivit using the polarization state-based method is identical wit that of spectral-based method, one can expect that spectral shifts can be further enlarged by careful engineering th

geometry of plasmonic nanostructures, and sensitivities exceeding 1000 nm/RIU can be possibly achieved.[22, 35] The resolution of ellipticity angle used to determine the line widths is 500 micro-radians, which is two-order larger than that of Maccaferri *et al.* used in the experiments.[57] Although theoretical line widths can be further reduced by enhancing the resolution of ellipticity angle, it should be noted that in addition to the resolution of the measurement system, the value of 1/*e* depends on the fabrication-induced errors in a realistic system, which could enlarge the line width of 1/*e* spectra. Besides that, the resolution of 500 micro-radians of the detection system is used to determine the line width of 1/*e* spectra in the calculations. However, a detection system with such a resolution may sustain high noise level, which could deteriorate the sensing performance. Therefore, the above mentioned issues must be considered in real experiments to achieve a large FoM. The polarization state of the incidence can be modified by ferromagnetic nanoparticles,[57] but plasmonic nanostructures could be more suitable for the polarization state-based sensing approach:

1) The sensing platform is simplified. The modulation of polarization state is achieved through magneto-optical effects for ferromagnetic nanoparticles, thereby a strong external magnetic field is required to implement the polarization state-based sensing. For plasmonic nanostructures, the polarization rotation and phase modulations are realized through charge transfer effect, and no external magnetic field is required in this case.

2) The sensing performance can be improved. The magneto-optical response of ferromagnetic nanoparticles is governed by the spin-orbit interactions and LSPRs, and the moment of transversally induced electric dipole is much weaker than that of the directly induced dipole, which means that the difference between the two components of electric field in Equ. (1) can be several orders of magnitude, and the sensing performance would be restricted for this reason. On the contrary, the moments of the generated orthogonal dipoles are comparable with each other for plasmonic nanostructures, and the polarization rotation and ellipticity are more sensitive to the incident wavelength around LSPRs, thereby the line width of 1/*e* spectrum can be reduced compared with that of ferromagnetic nanoparticles. Besides that, non-radiative losses of noble metals are weaker than that of ferromagnetic materials. It can help to generate strong near-field enhancement, leading to a large spectral shift with variations of surrounding medium. One can get improved sensing performance with plasmonic nanostructures.

3) The chemical stability is improved. Interactions between target molecules and sensing surface are important for label-free biosensing. Therefore, the chemical stability of the used material will affect the sensing performance. For ferromagnetic nanoparticles, the growth of an oxide layer could be an obstacle for the interactions with molecules. On the other hand, plasmonic materials such as gold possess a good chemical stability, and it can help to have better interactions with target molecules.

In order to implement the proposed polarization state-based sensing, two optical setups may be utilized: (1) the monochromatic light obtained with an acousto-optic tunable filter (AO filter) in the operation spectral range is passing through a polarizer to get linearly polarized beam, then the polarization state is modified by illuminating the sample with the light beam, after that the polarization state of transmitted field is analyzed with a polarization modulation technique, where the transmitted field is passing through a photoelastic modulator (PEM) and a polarizer before the intensity is measured with a photodetector, and the ellipticity is determined by filtering out the photoelastic signal with a lock-in amplifier;[44, 57, 71] (2) the sample is excited with a linearly polarized broadband continuum light source, then the transmitted field is passing through a Wollaston prism to separate the incidence into two orthogonal linearly polarized outgoing beams, after that the intensities of the two beams are measured with a spectrometer, and the whole ellipticity spectrum can be determined by rotating the Wollaston prism. In addition to the home-built setups, there are many commercially available polarization analyzers, such as the SOPRALAB GESP 5, the Adaptif Photonics A1000 and the Agilent 8509 series polarization analyzer, where the measurement rate of the latter one can be as high as 300 polarization states per second. Even higher speed polarization analyzers can be realized by careful engineering the optical setups.[72, 73] These high-speed polarization analyzers may be used to achieve real-time sensing by monitoring the polarization states.

Conclusions

In conclusion, polarization state-based refractive index sensing with plasmonic nanostructures have been studied in this paper. Instead of the intensity-based spectra, variations of the surrounding medium are analyzed by monitoring the polarization state of transmitted field, and the sensing performance characterized by FoM is significantly improved. It is shown that a linearly polarized wave transmitted through plasmonic nanostructures can become elliptical due to the charge transfer effect, which is governed by plasmon resonances. Therefore, a null condition with ellipticity approaching to zero is realized by manipulating the incident wavelength, and the ellipticity changes dramatically around the same spectral range. By plotting the spectra of the reciprocal of ellipticity, sharp resonances with line widths down to sub-nanometer are achieved, and the quality factor can be as large as several thousand. By manipulating the refractive index of surrounding medium, FoM exceeding 170 is achieved, and the performance of label-free biosensing can be dramatically improved.

Methods

The optical responses of the designed sensing platforms are calculated using the finite-difference time-domain method

(FDTD). The plasmonic nanostructures are placed on a semi-infinite glass substrate with the refractive index n = 1.45, and the complex dielectric constants of gold are taken from measured data.[74] Periodic boundary conditions around a unit cell are used to simulate the array of the plasmonic nanostructures, and perfectly matched layers are used on the other two sides to simulate the open space. During the FDTD calculations, a broadband plane wave pulse (700 – 1700 nm) with normal incidence is launched into the box containing the target structures to simulate a propagating plane wave interacting with the nanostructures. In order to precisely determine the spectral line widths using the polarization state-based method, the spectra are recalculated around the LSPRs with a wavelength resolution of 0.05 nm.

Acknowledgements

This work was supported by the National Natural Science Foundation of China (11304219, 11574228, and 61471254), the Project of International Cooperation of Shanxi Province (2015081025), and the Program for the Top Young Academic Leaders of Higher Learning Institutions of Shanxi.

Notes and references

1 S. A. Maier, *Plasmonics: fundamentals and applications*, Springer Science & Business Media, 2007.
2 P. K. Jain, K. S. Lee, I. H. El-Sayed and M. A. El-Sayed, *J. Phys. Chem. B*, 2006, **110**, 7238-7248.
3 X. Zhuo, X. Zhu, Q. Li, Z. Yang and J. Wang, *ACS nano*, 2015, **9**, 7523-7535.
4 A. J. Haes and R. P. Van Duyne, *J. Am. Chem. Soc.*, 2002, **124**, 10596-10604.
5 N. Nath and A. Chilkoti, *Anal. Chem.*, 2002, **74**, 504-509.
6 M. E. Stewart, C. R. Anderton, L. B. Thompson, J. Maria, S. K. Gray, J. A. Rogers and R. G. Nuzzo, *Chem. Rev.*, 2008, **108**, 494-521.
7 N. Li, A. Tittl, S. Yue, H. Giessen, C. Song, B. Q. Ding and N. Liu, *Light-Sci. Appl.*, 2014, **3**, e226.
8 L. J. Sherry, S. H. Chang, G. C. Schatz, R. P. Van Duyne, B. J. Wiley and Y. Xia, *Nano Lett.*, 2005, **5**, 2034-2038.
9 H. Gao, J. Henzie, M. H. Lee and T. W. Odom, *Proc. Natl. Acad. Sci. U. S. A.*, 2008, **105**, 20146-20151.
10 C. L. Nehl, H. Liao and J. H. Hafner, *Nano Lett.*, 2006, **6**, 683-688.
11 N. Zhou, C. Ye, L. Polavarapu and Q. H. Xu, *Nanoscale*, 2015, **7**, 9025-9032.
12 J. Becker, A. Trugler, A. Jakab, U. Hohenester and C. Sonnichsen, *Plasmonics*, 2010, **5**, 161-167.
13 L. Shao, Q. Ruan, R. Jiang and J. Wang, *Small*, 2014, **10**, 802-811.
14 S. C. Yang, J. L. Hou, A. Finn, A. Kumar, Y. Ge and W. J. Fischer, *Nanoscale*, 2015, **7**, 5760-5766.
15 B. Xue, D. Wang, J. Zuo, X. Kong, Y. Zhang, X. Liu, L. Tu, Y. Chang, C. Li, F. Wu, Q. Zeng, H. Zhao, H. Zhao and H. Zhang, *Nanoscale*, 2015, **7**, 8048-8057.
16 L. Feuz, M. P. Jonsson and F. Hook, *Nano Lett.*, 2012, **12**, 873-879.
17 J. B. Zeng, Y. Y. Cao, J. J. Chen, X. D. Wang, J. F. Yu, B. B. Yu, Z. F. Yan and X. Chen, *Nanoscale*, 2014, **6**, 9939-9943.
18 E. M. Larsson, J. Alegret, M. Kall and D. S. Sutherland, *Nano Lett.*, 2007, **7**, 1256-1263.
19 X. Xu, B. Peng, D. Li, J. Zhang, L. M. Wong, Q. Zhang, S. Wang and Q. Xiong, *Nano Lett.*, 2011, **11**, 3232-3238.
20 I. M. Pryce, Y. A. Kelaita, K. Aydin and H. A. Atwater, *ACS nano*, 2011, **5**, 8167-8174.
21 J. Zhao, C. Zhang, P. V. Braun and H. Giessen, *Adv. Mater.*, 2012, **24**, OP247-OP252.
22 W. Kubo and S. Fujikawa, *Nano Lett.*, 2011, **11**, 8-15.
23 S. Zhang, D. A. Genov, Y. Wang, M. Liu and X. Zhang, *Phys. Rev. Lett.*, 2008, **101**, 047401.
24 N. Verellen, Y. Sonnefraud, H. Sobhani, F. Hao, V. V. Moshchalkov, P. Van Dorpe, P. Nordlander and S. A. Maier, *Nano Lett.*, 2009, **9**, 1663-1667.
25 Z. Fang, J. Cai, Z. Yan, P. Nordlander, N. J. Halas and X. Zhu, *Nano Lett.*, 2011, **11**, 4475-4479.
26 J. A. Fan, C. Wu, K. Bao, J. Bao, R. Bardhan, N. J. Halas, V. N. Manoharan, P. Nordlander, G. Shvets and F. Capasso, *Science*, 2010, **328**, 1135-1138.
27 Z. Li, S. Zhang, L. Tong, P. Wang, B. Dong and H. Xu, *ACS nano*, 2014, **8**, 701-708.
28 Z. J. Yang, Z. H. Hao, H. Q. Lin and Q. Q. Wang, *Nanoscale*, 2014, **6**, 4985-4997.
29 Y. Bao, Z. Hu, Z. Li, X. Zhu and Z. Fang, *Small*, 2015, **11**, 2177-2181.
30 N. Liu, S. Mukherjee, K. Bao, L. V. Brown, J. Dorfmuller, P. Nordlander and N. J. Halas, *Nano Lett.*, 2012, **12**, 364-369.
31 S. D. Liu, Z. Yang, R. P. Liu and X. Y. Li, *ACS nano*, 2012, **6**, 6260-6271.
32 B. Gallinet and O. J. Martin, *ACS nano*, 2013, **7**, 6978-6987.
33 Y. Sonnefraud, N. Verellen, H. Sobhani, G. A. Vandenbosch, V. V. Moshchalkov, P. Van Dorpe, P. Nordlander and S. A. Maier, *ACS nano*, 2010, **4**, 1664-1670.
34 F. Hao, P. Nordlander, Y. Sonnefraud, P. Van Dorpe and S. A. Maier, *ACS nano*, 2009, **3**, 643-652.
35 N. Verellen, P. Van Dorpe, C. Huang, K. Lodewijks, G. A. Vandenbosch, L. Lagae and V. V. Moshchalkov, *Nano Lett.*, 2011, **11**, 391-397.
36 Y. Zhan, D. Y. Lei, X. Li and S. A. Maier, *Nanoscale*, 2014, **6**, 4705-4715.
37 S. Zhang, K. Bao, N. J. Halas, H. Xu and P. Nordlander, *Nano Lett.*, 2011, **11**, 1657-1663.
38 F. Lopez-Tejeira, R. Paniagua-Dominguez and J. A. Sanchez-Gil, *ACS nano*, 2012, **6**, 8989-8996.
39 Y. H. Fu, J. B. Zhang, Y. F. Yu and B. Luk'yanchuk, *ACS nano*, 2012, **6**, 5130-5137.
40 C. Wu, A. B. Khanikaev, R. Adato, N. Arju, A. A. Yanik, H. Altug and G. Shvets, *Nat. Mater.*, 2012, **11**, 69-75.
41 A. A. Yanik, A. E. Cetin, M. Huang, A. Artar, S. H. Mousavi, A. Khanikaev, J. H. Connor, G. Shvets and H. Altug, *Proc. Natl. Acad. Sci. U. S. A.*, 2011, **108**, 11784-11789.
42 Y. Yang, Kravchenko, II, D. P. Briggs and J. Valentine, *Nat. Commun.*, 2014, **5**, 5753.
43 S. Seo, M. R. Gartia and G. L. Liu, *Nanoscale*, 2014, **6**, 11795-11802.
44 K. Lodewijks, W. Van Roy, G. Borghs, L. Lagae and P. Van Dorpe, *Nano Lett.*, 2012, **12**, 1655-1659.
45 W. Y. Chen, C. H. Lin and W. T. Chen, *Nanoscale*, 2013, **5**, 9950-9956.
46 N. Liu, M. Mesch, T. Weiss, M. Hentschel and H. Giessen, *Nano Lett.*, 2010, **10**, 2342-2348.
47 Y. Gao, Z. Xin, B. Zeng, Q. Gan, X. Cheng and F. J. Bartoli, *Lab on a chip*, 2013, **13**, 4755-4764.
48 Y. Gao, Q. Gan, Z. Xin, X. Cheng and F. J. Bartoli, *ACS nano*, 2011, **5**, 9836-9844.
49 Y. Gao, Z. Xin, Q. Gan, X. Cheng and F. J. Bartoli, *Opt. Express*, 2013, **21**, 5859-5871.
50 Q. Gan, Y. Gao and F. J. Bartoli, *Opt. Express*, 2009, **17**, 20747-20755.
51 L. Lin and Y. Zheng, *Nanoscale*, 2015, **7**, 12205-12214.

52 M. Bahramipanah, S. Dutta-Gupta, B. Abasahl and O. J. Martin, *ACS nano*, 2015, **9**, 7621-7633.
53 A. E. Cetin and H. Altug, *ACS nano*, 2012, **6**, 9989-9995.
54 K. Lodewijks, J. Ryken, W. Van Roy, G. Borghs, L. Lagae and P. Van Dorpe, *Plasmonics*, 2013, **8**, 1379-1385.
55 P. Offermans, M. C. Schaafsma, S. R. K. Rodriguez, Y. Zhang, M. Crego-Calama, S. H. Brongersma and J. Gómez Rivas, *ACS nano*, 2011, **5**, 5151-5157.
56 Y. Shen, J. Zhou, T. Liu, Y. Tao, R. Jiang, M. Liu, G. Xiao, J. Zhu, Z. K. Zhou, X. Wang, C. Jin and J. Wang, *Nat. Commun.*, 2013, **4**, 2381.
57 N. Maccaferri, K. E. Gregorczyk, T. V. de Oliveira, M. Kataja, S. van Dijken, Z. Pirzadeh, A. Dmitriev, J. Akerman, M. Knez and P. Vavassori, *Nat. Commun.*, 2015, **6**, 6150.
58 J. K. Gansel, M. Thiel, M. S. Rill, M. Decker, K. Bade, V. Saile, G. von Freymann, S. Linden and M. Wegener, *Science*, 2009, **325**, 1513-1515.
59 A. Drezet, C. Genet and T. W. Ebbesen, *Phys. Rev. Lett.*, 2008, **101**, 043902.
60 L. J. Black, Y. Wang, C. H. de Groot, A. Arbouet and O. L. Muskens, *ACS nano*, 2014, **8**, 6390-6399.
61 X. Lu, J. Wu, Q. Zhu, J. Zhao, Q. Wang, L. Zhan and W. Ni, *Nanoscale*, 2014, **6**, 14244-14253.
62 S. Wu, Z. Zhang, Y. Zhang, K. Y. Zhang, L. Zhou, X. J. Zhang and Y. Y. Zhu, *Phys. Rev. Lett.*, 2013, **110**, 207401.
63 F. Ding, Z. Wang, S. He, V. M. Shalaev and A. V. Kildishev, *ACS nano*, 2015, **9**, 4111-4119.
64 T. Li, S. M. Wang, J. X. Cao, H. Liu and S. N. Zhu, *Appl. Phys. Lett.*, 2010, **97**, 261113.
65 E. Prodan, C. Radloff, N. J. Halas and P. Nordlander, *Science*, 2003, **302**, 419-422.
66 M. Konig, M. Rahmani, L. Zhang, D. Y. Lei, T. R. Roschuk, V. Giannini, C. W. Qiu, M. Hong, S. Schlucker and S. A. Maier, *ACS nano*, 2014, **8**, 9188-9198.
67 W. H. Zhang and O. J. F. Martin, *Acs Photonics*, 2015, **2**, 144-150.
68 J. Q. Li, J. Ye, C. Chen, Y. Li, N. Verellen, V. V. Moshchalkov, L. Lagae and P. Van Dorpe, *Acs Photonics*, 2015, **2**, 425-431.
69 M. Svedendahl, S. Chen, A. Dmitriev and M. Kall, *Nano Lett.*, 2009, **9**, 4428-4433.
70 S. M. George, *Chem. Rev.*, 2010, **110**, 111-131.
71 P. Vavassori, *Appl. Phys. Lett.*, 2000, **77**, 1605.
72 G. D. Van Wiggeren and R. Roy, *Opt. Commun.*, 1999, **164**, 107-120.
73 L. S. Yan, X. S. Yao, C. Yu, Y. Wang, L. Lin, Z. Chen and A. E. Willner, *IEEE Photonic Tech. L.*, 2006, **18**, 643-645.
74 P. B. Johnson and R. W. Christy, *Phys. Rev. B*, 1972, **6**, 4370-4379.